Piezoelectric sensor characterization for structural strain measurements

Ghaderiaram, Aliakbar; Vafa, Navid; Schlangen, Erik; Fotouhi, Mohammad

DOI
10.1016/j.sna.2025.116659

Publication date
2025

Document Version
Final published version

Published in
Sensors and Actuators A: Physical

Sensors & Actuators: A. Physical 391 (2025) 116659

Contents lists available at ScienceDirect

Sensors and Actuators: A. Physical

journal homepage: www.journals.elsevier.com/sensors-and-actuators-a-physical

Piezoelectric sensor characterization for structural strain measurements

Aliakbar Ghaderiaram *, Navid Vafa, Erik Schlangen, Mohammad Fotouhi

The Delft University of Technology, Delft 2628CN, the Netherlands

ARTICLE INFO

Keywords:
Piezoelectric sensor
PZT
PVDF
Uniaxial strain
Attachment
Shear leg
Poisson's ratio

ABSTRACT

Accurate and reliable strain measurement is essential for effective condition monitoring of engineering structures. This study presents an analytical and experimental investigation into the performance of piezoelectric sensors for structural strain measurements, evaluating the effect of attachment strategy and the properties of the substrate and the sensor. Lead zirconate titanate (PZT) and polyvinylidene fluoride (PVDF) sensors were evaluated in two attachment configurations: Fully Attached (FA) and Two-End Attached (TEA). A voltage-strain relationship was developed based on principles of piezoelectricity, electrical circuit modelling, and solid mechanics. Results indicate that sensor performance is significantly influenced by the attachment method. Specifically, the TEA configuration reduced the impact of substrate properties and improved uniaxial strain measurement accuracy by up to 32 % compared to the FA configuration. The FA configuration exhibited sensitivity to the substrate's Poisson ratio, leading to a nonlinear voltage-strain response. In contrast, the TEA configuration provided pure uniaxial strain measurements by reducing the effects of shear lag and substrate elasticity. These findings provide a comprehensive approach to using piezoelectric sensors for structural strain measurement, allowing for the placement of sensors on various substrates without the need for calibration by effectively utilizing sensor and substrate properties along with the attachment strategy. The study provides a novel analytical–experimental comparison of sensor attachment methods, showing how TEA significantly improves uniaxial strain accuracy and reduces substrate dependency in piezoelectric strain measurements.

1. Introduction

Ensuring the safety and reliability of engineering structures necessitates cautious monitoring of their strain history. While various strain measurement techniques exist, challenges such as substrate dependency, shear lag effect, and sensor attachment constraints limit their effectiveness in real-world applications. For example, cyclic strains due to in-service loadings can lead to fatigue failure which is a gradual, localized process that accumulates over time in different engineering structures such as bridges [1,2], high-rise buildings [3], and offshore platforms [4]. These cyclic strains are significantly lower than the structure's strain to failure; however, they can lead to structural failure or dysfunction over time [5,6]. It is therefore essential to develop reliable and accurate strain measurement solutions.

Traditionally, a variety of strain measurement techniques, such as strain gauges [7], Linear Variable Differential Transformers (LVDTs) [8], extensometers [9], Fiber Bragg Gratings (FBGs) [10], Digital Image Correlation (DIC) [11], and accelerometer [12], have been used to monitor cyclic strain in structures. While these methods are widely used, they each have limitations. For instance, FBGs are prone to brittleness and installation complexity, while DIC requires precise surface preparation and can be affected by resolution challenges in practical applications. These issues can hinder the reliability of long-term structural health monitoring. Recent advances in flexible pressure sensors, including resistive, capacitive, and piezoelectric types, have also highlighted challenges such as mechanical mismatch, hysteresis, and signal drift that similarly affect long-term sensing reliability [13–15].

Piezoelectric sensors have emerged as a promising alternative for strain measurement. While piezoelectric sensors are primarily used in high-frequency applications such as ultrasonic testing [16–18], acoustic emission [19,20], and electromechanical impedance measurements [21,22], their ability to generate electrical displacement in response to mechanical strain makes them suitable for use as strain gauges [23,24]. Piezoelectric sensors offer a higher signal-to-noise ratio and greater sensitivity in a higher frequency range than traditional strain gauges [25]. These sensors operate in a passive mode, eliminating the need for an external power source and requiring less complex electronics [26], and offer higher sensitivity, especially in low-strain and high-noise

* Corresponding author.
E-mail address: a.ghaderiaram@tudelft.nl (A. Ghaderiaram).

https://doi.org/10.1016/j.sna.2025.116659
Received 22 October 2024; Received in revised form 23 April 2025; Accepted 2 May 2025
Available online 3 May 2025

dynamic loadings, compared to traditional strain gauges [25,27]. Additionally, they can simultaneously detect longitudinal and transverse strains, making them versatile in capturing multi-directional strain responses.

However, despite their advantages, the use of piezoelectric sensors in structural strain measurement comes with its own set of challenges, including a limited strain range, sensitivity to the substrate's mechanical properties—particularly Poisson's ratio and potential inaccuracies due to incomplete strain transfer to the sensor caused by the shear lag effect in the bonding layer between the sensor and the substrate [25,28]. For example, Lead zirconate titanate (PZT) sensors are not ideal for measuring strains exceeding 100–150 με due to potential nonlinearities and changes in material properties, which can compromise calibration accuracy [25,29]. However, experimental results have reported maximum strain measurements of 1 % [30] to 3.5 % [31], though the linear elastic region remains very limited. Unlike traditional resistive strain gauges—which are primarily sensitive to unidirectional strain—piezoelectric sensors respond to both longitudinal and transverse strains [25,32]. As a result, at least two piezoelectric sensors are typically required to distinguish uniaxial strain accurately.

To overcome these limitations and better understand the behaviour of piezoelectric sensors, this study aims to characterize two piezoelectric materials: PZT and polyvinylidene fluoride (PVDF), both commonly used in sensing applications. The performance of these sensors is analysed in two distinct bonding configurations: Fully Attached (FA) and Two-End Attached (TEA). The FA configuration ensures full contact between the sensor and the substrate, while the TEA configuration reduces the bonding area to two ends, which could help minimize the influence of the substrate's mechanical properties. This research provides practical insights into optimizing piezoelectric sensor configurations for structural health monitoring applications, ultimately offering a more accurate and reliable approach to strain measurement in engineering structures.

This study uniquely combines analytical modelling and experimental validation to evaluate the performance of piezoelectric strain sensors under two attachment configurations (FA and TEA). The findings demonstrate how attachment strategy influences sensor sensitivity, strain transfer efficiency, and dependency on substrate properties, offering a practical framework for accurate strain measurement using piezoelectric sensors across diverse structural materials.

2. Materials and methods

The detailed properties of PZT and PVDF sensors are provided in Table 1. The PZT was a P-876.A11 soft piezoelectric sensor, made from PIC255 piezo-ceramic and manufactured by PI Company. A stainless steel strip with 250 × 55 × 1.5 mm dimensions was used as the substrate structure. Cyanoacrylate glue was applied to mount the piezoelectric sensors to the structure. Please note that the PVDF sensor was only studied analytically.

Table 1
Piezoelectric sensors and substrate properties.

Property	Qty	Unit
Min. lateral contraction (PZT)	650	$\mu m/m$
Poisson ratio (PZT)	0.35	
Young's moduli $E_1=E_2$ (PIC255) [33]	63E9	Nm^{-2}
Young's modulus (PZT sensor)	16.4E9	Nm^{-2}
$d_{31} = d_{32}$ (PZT)	−175E−12	CN^{-1}
d_{31} (PVDF) [34]	23E−12	CN^{-1}
Young's modulus$_{(x)}$ (PVDF sensor)	2–4E9	Nm^{-2}
Poisson ratio$_{(x)}$ (PVDF)	0.3	
a_r (PVDF) [35]	0.6	
d_r (PVDF)	0.22	
Young's modulus$_{(x)}$ (stainless steel) [36]	200E9	Nm^{-2}
Poisson ratio (stainless steel)	0.27	
G (glue)	25E6	Nm^{-2}

Fig. 1 illustrates a series of cyclic uniaxial tensile loads applied to the substrate within its linear elastic range using an Instron machine. The loading consisted of sinusoidal cycles, ranging from a minimum of 0.2 kN to a maximum of 12 kN. The amplitude of these cycles was adjusted to four specific levels: 2 kN, 4 kN, 8 kN, and 12 kN. The loading frequency was varied between 0.5 Hz and 4 Hz, with intermediate frequencies of 1 Hz, 2 Hz, and 3 Hz. During the tests, the output signals of both PZT piezoelectric sensors were recorded using a digital oscilloscope with a sampling rate of 1 GSa/s. DIC was used to monitor strain variations within both the sensors and the substrate. To enhance the accuracy of strain measurement using DIC, the surfaces of both the substrate and the sensors were patterned with a grid of small, randomly distributed speckle patterns. These patterns create unique image features that can be tracked and correlated between different images, allowing for precise determination of surface displacements and strains.

3. Voltage-strain relationship in piezoelectric materials

3.1. Piezoelectricity

Piezoelectric materials produce an electric charge when subjected to mechanical stress or deformation. Fig. 2 illustrates a 2D configuration of a quartz crystal in different states. In its undeformed state, the positive charge center (C_Q^+) and the negative charge center (C_Q^-) are perfectly aligned, resulting in electrical neutrality. However, these charge centres shift apart when mechanical deformation occurs, creating electric dipole moments between C_Q^- and C_Q^+. This separation leads to polarization, represented by P, which increases as the distance between C_Q^- and C_Q^+ grows. If the electrodes are short-circuited, an electric current flows due to the charge movement. Alternatively, when the electrodes are electrically isolated, a voltage difference can be measured, demonstrating the complex relationship between mechanical forces and electrical behaviour in piezoelectric materials [37].

Piezoelectric materials generally convert mechanical deformation into an electrical field, and vice versa, as described by the piezoelectric duality [37,38] relevant variables are outlined in Table 2. The superscripts S and E indicate that the quantity is measured at constant strain and constant electric field, respectively. The subscripts $\{i, j, k, l, m, n\}$ refer to spatial directions $\{x, y, z\}$ or $\{1, 2, 3\}$.

$$\begin{aligned} D_m &= \varepsilon^T_{mn} E_n + d_{mkl} T_{kl} \\ S_{ij} &= d_{ijn} E_n + s^E_{ijkl} T_{kl} \end{aligned} \tag{1}$$

Eq. 1 consists of two components: the mechanically induced electric field (D_m), and the electrically induced mechanical deformation (S_{ij}), which can also function as an actuator. In this study, the piezoelectric is used as a sensor, so only the first component must be investigated. In the first component, two different sources contribute to the electrical displacement. The electric field E_n can either originate from an external power source or the local electric field generated by mechanically induced electrical displacement. Since this study employs the piezoelectric sensor as a passive sensor, there is no external power source, and the electric field generated by the mechanically induced displacement is negligible. Therefore, the vector of electrical displacement can be simplified to the mechanically induced component and is expressed in matrix form in Eq. 2.

$$\begin{bmatrix} D_1 \\ D_2 \\ D_3 \end{bmatrix} = \begin{bmatrix} d_{11} & d_{12} & d_{13} & d_{14} & d_{15} & d_{16} \\ d_{21} & d_{22} & d_{23} & d_{24} & d_{25} & d_{26} \\ d_{31} & d_{32} & d_{33} & d_{34} & d_{35} & d_{36} \end{bmatrix} \begin{bmatrix} T_{11} \\ T_{22} \\ T_{33} \\ T_{23} \\ T_{13} \\ T_{12} \end{bmatrix} \tag{2}$$

The tensor of the piezoelectric stress constant can be simplified depending on the symmetry of the piezoelectric material. For the PIC255 PZT piezoelectric material used in this study, which falls under crystal class 6 mm, certain symmetries exist [39]. As a result, several tensor

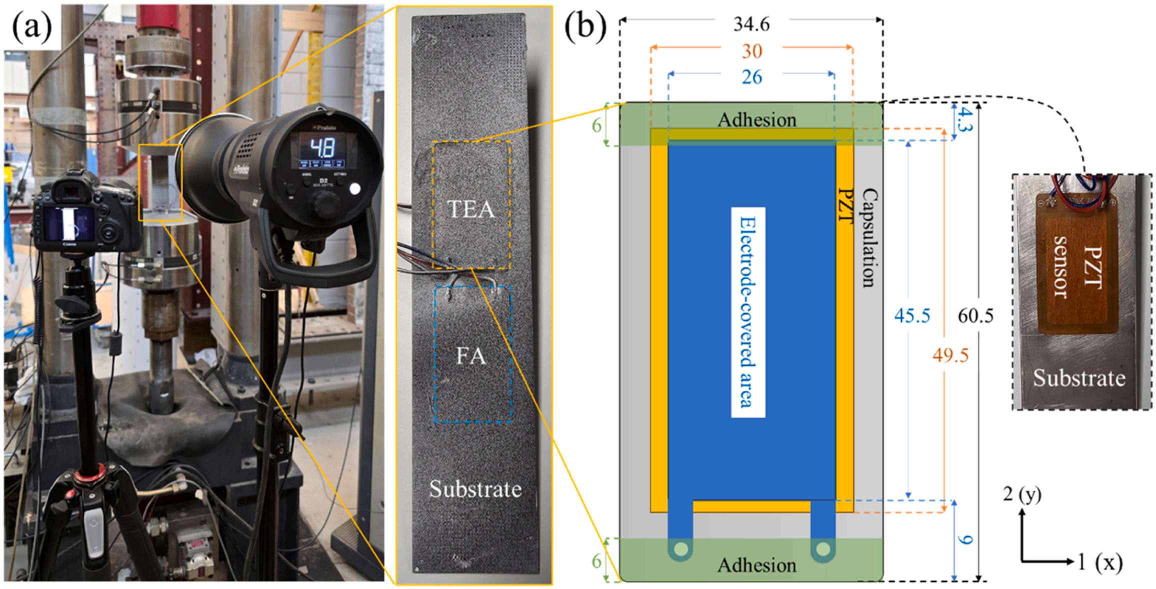

Fig. 1. (a) A tension-tension test setup with DIC measurements, including PZT sensors in FA and TEA configurations, (b) PZT sensor dimensions and an adhesive layer for TEA.

entries are zero, leading to a simplified form, as shown in Eq. 3.

$$\begin{bmatrix} D_1 \\ D_2 \\ D_3 \end{bmatrix} = \begin{bmatrix} 0 & 0 & 0 & 0 & d_{15} & 0 \\ 0 & 0 & 0 & d_{24} & 0 & 0 \\ d_{31} & d_{32} & d_{33} & 0 & 0 & 0 \end{bmatrix} \begin{bmatrix} T_{11} \\ T_{22} \\ T_{33} \\ T_{23} \\ T_{13} \\ T_{12} \end{bmatrix} \tag{2}$$

The coefficients d_{31}, d_{32} and d_{33} represent the normal strains in the coordinate directions relative to the poling direction, which is perpendicular to the electrode plane (along the 3-axis). The other coefficients, d_{15} and d_{24}, correspond to shear strains in the 1–3 and 2–3 planes, respectively, contributing to the electric field in the 1 and 2 directions. However, for a piezoelectric film poled in the 3 direction, shear in the 1–2 plane does not contribute to the generation of any electric displacement [25,39]. To obtain the overall generated electric charge, Eq. 3 can be used:

$$q = \iiint \begin{bmatrix} D_1 & D_2 & D_3 \end{bmatrix} \begin{bmatrix} dA_1 \\ dA_2 \\ dA_3 \end{bmatrix} \tag{3}$$

Where dA_n is the plane perpendicular to direction n. It is important to note that electrodes are required to collect electric charges from each plane. In the piezoelectric sensor used in this study, the electrodes are fabricated on the 1–2 plane (or in the 3 direction, through the thickness). As a result, only the electrical displacement D_3 contributes to the collected electric charge. Here A is the area covered by electrodes:

$$q = D_3 \times A \tag{4}$$

To relate the system to a more practical parameter, such as electrical current, the rate of change of electric charge q is described in Eq. 5:

$$I_D = \frac{dq_{(t)}}{dt} = \frac{dAD_3}{dt} = A\frac{dD_3}{dt} \tag{5}$$

3.1.1. The equivalent electrical circuit of a piezoelectric

The behaviour of a piezoelectric sensor can be represented by an equivalent circuit, commonly known as Van Dyke's Model [40]. Given the wide range of applications and operating frequencies of piezoelectric sensors, more complex models have been developed to account for higher-order resonance frequencies and dynamic behaviour [41].

Fig. 3a presents a simplified yet comprehensive model of a piezoelectric sensor, incorporating both resonant and non-resonant components [42], as well as a current source based on electrical displacement. This model distinguishes between the resonant and non-resonant parts, each dominating specific frequency ranges depending on the piezoelectric properties. In comparison, the resistance R_p is significantly higher than R_s and R_m. At resonance, the impedance of L_m and C_m cancels out, resulting in zero net impedance, with $R_m$being the dominant impedance in the circuit. However, at lower frequencies, the impedance of the resonant branch becomes much larger than the other branches, so its effect is negligible. Additionally, at frequencies below 100 Hz, the impedance of capacitor C is much higher than that of R_s, allowing R_s to be disregarded. Under these assumptions, the equivalent circuit simplifies to a parallel combination of R_p and C, along with the current source I_D, as shown in Fig. 3b. R_L represents the external load resistor, which could originate from measurement equipment or specific electronic circuits [43]. The two parallel resistors can be replaced by an equivalent resistor R, as illustrated in Fig. 3c and calculated using Eq. 6.

$$R = R_p || R_L = \frac{R_p \times R_L}{R_p + R_L} \tag{6}$$

The circuit is reduced to a first-order parallel RC configuration, as described in Eq. 7. The capacitor C represents the inherent capacitance of the piezoelectric sensor. This capacitance is determined by the sensor's physical dimensions and piezoelectric material properties.

$$C = \frac{\varepsilon_0 \varepsilon_r A}{h_{pzt}} \tag{7}$$

Where $\varepsilon_0$andε_r are the vacuum and relative permittivity, d is the distance between two electrodes, A is the covered area between two electrodes, and h_{pzt} and ϑ are the thickness and Poisson's ratio of piezoelectric material.

Kirchhoff's current law is applied to solve the RC circuit and determine the sensor's output voltage as a function of electrical displacement, as shown in Eq. 8, for the current in the circuit depicted in Fig. 3c.

$$I_D = i_c + i_R \tag{8}$$

Where i_R follows Ohm's law, and the current through the capacitor can be described by Eq. 9, based on Coulomb's law.

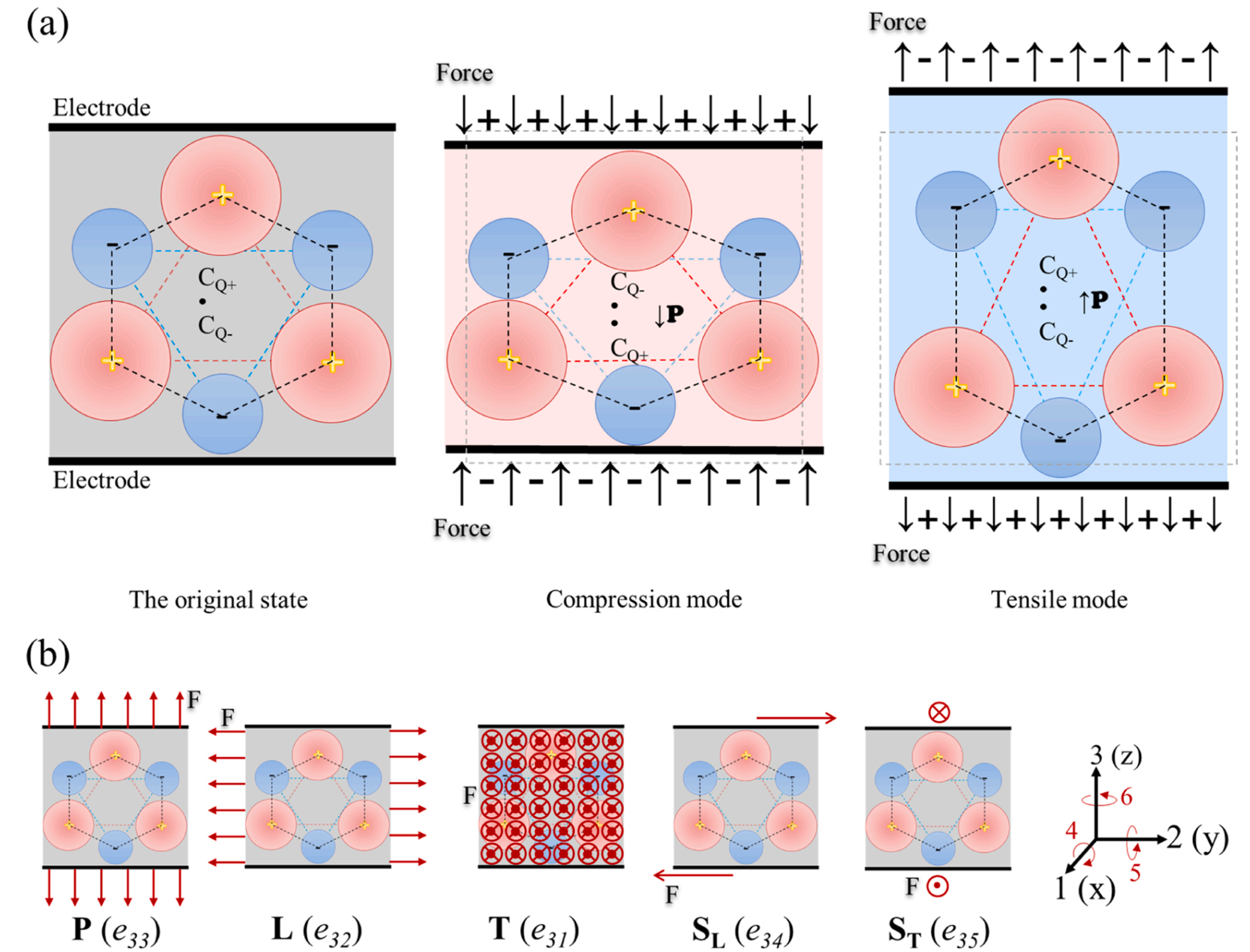

Fig. 2. (a) Schematic of a 2D piezoelectric lattice with electrodes on both x–y surfaces, illustrating charge center alignment in three distinct mechanical load states; (b) Loading directions relevant to piezoelectric behaviour, including normal load (P), longitudinal (L), transverse (T), longitudinal shear (SL), and transverse shear (ST).

Table 2
Variables used in Eq. 1.

Notation	Description	Unit
Intensive state variables		
E_n	Electric field density; vector	Vm^{-1}
T_{kl}	Mechanical stress; tensor rank 2	Nm^{-2}
Extensive state variables		
D_m	Electric flux density; vector	Cm^2
S_{ij}	Mechanical strain; tensor rank 2	-
Material parameter		
$\varepsilon^{T,\vartheta}_{mn}$	Electric permittivity; tensor rank 2	$AsV^{-1}m^{-1}$; Fm^{-1}
d_{mkl}	Piezoelectric strain constants; tensor rank 3	Cm^{-2}; $NV^{-1}\ m^{-1}$
$s^{E,\vartheta}_{ijkl}$	Elastic compliance constants; tensor rank 4	m^2N^{-1}

$$Q = C.V \quad , \quad i = \frac{dQ}{dt} \quad \rightarrow \quad i_c = C\frac{dv}{dt} \tag{9}$$

Where $v = v_{out}$ in circuit Fig. 3c. Substituting the expressions for the currents into Eq. 8 results in a first-order differential equation, as shown in Eq. 10.

$$\frac{dv}{dt} + \frac{v}{R.C} - \frac{A}{C}\ \frac{dD_3}{dt} \quad = 0 \tag{10}$$

Considering the initial conditions as zero (since the external power source is not connected to the sensor), the voltage generated by the piezoelectric sensor can be described by Eq. 11.

$$v_{(t)} = \frac{A}{C} e^{\frac{-t}{\tau}} \int_0^T e^{\frac{t}{\tau}}\ \frac{dD_3}{dt} dt \tag{11}$$

Where τ=RC is defined as the time constant of the piezoelectric sensor. This τ characterizes the speed at which the sensor discharges, or more specifically, the recombination rate of the generated charge, reflecting the system's tendency to return to equilibrium under static loading conditions.

From Eq. 11, it becomes clear that the generated voltage is directly proportional to the rate of electrical displacement, meaning that the sensor is particularly sensitive to dynamic deformations, while its response to static or slow-changing loads is minimal.

In the following section, the connection between the mechanical strain and electrical displacement is described.

3.2. Strain distributions

3.2.1. Strain in FA piezoelectric sensor

The substrate is assumed to be in a state of plane stress, a condition

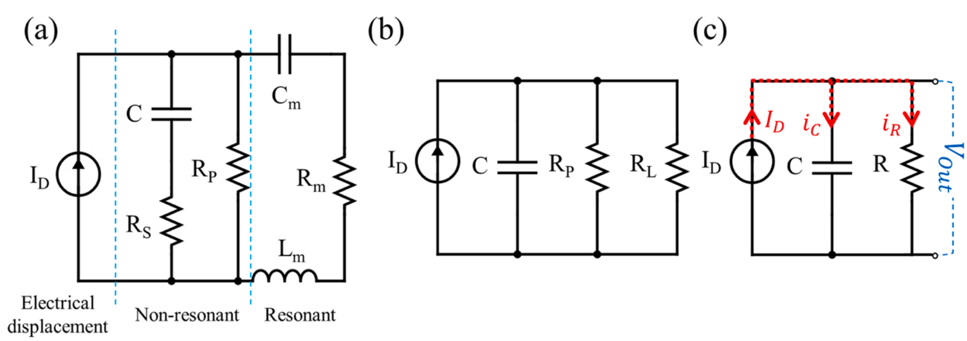

Fig. 3. Equivalent electrical circuit models of a piezoelectric sensor: (a) full circuit representation valid across a wide frequency range, (b) simplified model for low-frequency operation ($f \ll f_r$), including the load resistor RL, and (c) further reduced circuit with an equivalent parallel resistance.

commonly found in thin plates where the out-of-plane stresses are minimal [44]. Hooke's law, relating stress and strain through Young's modulus and Poisson's ratio (Eq. 12), will be applied to analyse strain distribution and its transfer to the attached piezoelectric sensor under mechanical loading.

$$\begin{cases} \varepsilon_{1ss} = \dfrac{\sigma_1}{E_{ss}} - \vartheta_{ss}\dfrac{\sigma_2}{E_{ss}} = -\vartheta_{ss}\dfrac{\sigma_2}{E_{ss}} \\ \varepsilon_{2ss} = -\vartheta_{ss}\dfrac{\sigma_1}{E_{ss}} + \dfrac{\sigma_2}{E_{ss}} = \dfrac{\sigma_2}{E_{ss}} \end{cases} \tag{12}$$

Where the subscript "ss" refers to the stainless steel substrate. Under the uniaxial test condition shown in Fig. 1, only σ_2 is present, while the strain in the 1(x)-direction is controlled by Poisson's ratio, reflecting the material's lateral contraction or expansion. In the FA configuration of the PZT piezoelectric sensor, and under the assumption of an ideal (rigid and thin) bonding layer and lateral isotropy in the PZT material, the sensor is assumed to experience approximately the same in-plane strain as the substrate. However, in practical conditions, this strain transfer is affected by the shear lag effect, which is addressed later in this section. Additionally, the plane stress condition applies to the sensor, meaning out-of-plane stresses are negligible, and in-plane strains dominate its response [45].

Considering the isotropy of the PZT material and the strain transferred from the substrate, the axial stress in the PZT piezoelectric sensor is presented in Eq. 13.

$$\begin{bmatrix} T_{1_{PZT}} \\ T_{2_{PZT}} \end{bmatrix} = \frac{E_{PZT}}{(1-\vartheta_{PZT}{}^2)} \begin{bmatrix} 1 & \vartheta_{PZT} \\ \vartheta_{PZT} & 1 \end{bmatrix} \begin{bmatrix} \varepsilon_{1ss} \\ \varepsilon_{2ss} \end{bmatrix} = \frac{E_{PZT}}{(1-\vartheta_{PZT}{}^2)} \begin{bmatrix} 1 & \vartheta_{PZT} \\ \vartheta_{PZT} & 1 \end{bmatrix} \begin{bmatrix} -\vartheta_{ss}\dfrac{\sigma_2}{E_{ss}} \\ \dfrac{\sigma_2}{E_{ss}} \end{bmatrix} \tag{13}$$

$$T_{1_{PVDF}} = \frac{E_{1_{PVDF}}}{(1-\vartheta_{1_{PVDF}}\vartheta_{2_{PVDF}})}\left(-\vartheta_{ss}\frac{\sigma_2}{E_{ss}} + \vartheta_{1_{PVDF}}\frac{\sigma_2}{E_{ss}}\right) = \frac{E_{1_{PVDF}}}{(1-\vartheta_{1_{PVDF}}{}^2 a_r)}\left(\frac{\sigma_2}{E_{ss}}\right)(\vartheta_{1_{PVDF}} - \vartheta_{ss})$$
$$T_{2_{PVDF}} = \frac{E_{1_{PVDF}}}{(1-\vartheta_{1_{PVDF}}\vartheta_{2_{PVDF}})}\left(-\vartheta_{ss}\vartheta_{2_{PVDF}}\frac{\sigma_2}{E_{ss}} + \frac{E_{2_{PVDF}}}{E_{1_{PVDF}}}\frac{\sigma_2}{E_{ss}}\right) = \frac{E_{1_{PVDF}}}{(1-\vartheta_{1_{PVDF}}{}^2 a_r)}\left(\frac{\sigma_2}{E_{ss}}\right)(a_r - \vartheta_{2_{PVDF}}\vartheta_{ss}) \tag{16}$$

According to Eq. 2 and considering the equal piezoelectric coefficients in directions 1 and 2 for the PZT piezoelectric sensor (as shown in Table 1), increased axial stress results in greater electrical displacement. However, as presented in Eq. 14, for substrates with a lower Poisson's ratio, T_1 (transverse stress) becomes positive, enhancing the overall electrical displacement. Conversely, for substrates with a higher Poisson's ratio than the PZT sensor, T_1 becomes negative, reducing the total electrical displacement and consequently lowering the sensor's output voltage.

$$T_{1_{PZT}} = \frac{E_{PZT}}{(1-\vartheta_{PZT}{}^2)}\left(-\vartheta_{ss}\frac{\sigma_2}{E_{ss}} + \vartheta_{PZT}\frac{\sigma_2}{E_{ss}}\right) = \frac{E_{PZT}}{(1-\vartheta_{PZT}{}^2)}\left(\frac{\sigma_2}{E_{ss}}\right)(\vartheta_{PZT} - \vartheta_{ss})$$
$$T_{2_{PZT}} = \frac{E_{PZT}}{(1-\vartheta_{PZT}{}^2)}\left(-\vartheta_{ss}\vartheta_{PZT}\frac{\sigma_2}{E_{ss}} + \frac{\sigma_2}{E_{ss}}\right) = \frac{E_{PZT}}{(1-\vartheta_{PZT}{}^2)}\left(\frac{\sigma_2}{E_{ss}}\right)(1 - \vartheta_{PZT}\vartheta_{ss}) \tag{14}$$

For the PVDF piezoelectric sensor, due to its orthorhombic symmetry, Young's modulus and Poisson's ratio differ between the longitudinal and transversal directions [46–48]. As a result, the stress distribution in a PVDF sensor in the FA configuration is different from that of the PZT sensor, which is described by Eq. 15 [24].

$$\begin{bmatrix} T_{1_{PVDF}} \\ T_{2_{PVDF}} \end{bmatrix} = \frac{E_{1_{PVDF}}}{(1-\vartheta_{1_{PVDF}}\vartheta_{2_{PVDF}})} \begin{bmatrix} 1 & \vartheta_{1_{PVDF}} \\ \vartheta_{2_{PVDF}} & \dfrac{E_{2_{PVDF}}}{E_{1_{PVDF}}} \end{bmatrix} \begin{bmatrix} \varepsilon_{1ss} \\ \varepsilon_{2ss} \end{bmatrix} = \frac{E_{1_{PVDF}}}{(1-\vartheta_{1_{PVDF}}\vartheta_{2_{PVDF}})} \begin{bmatrix} 1 & \vartheta_{1_{PVDF}} \\ \vartheta_{2_{PVDF}} & \dfrac{E_{2_{PVDF}}}{E_{1_{PVDF}}} \end{bmatrix} \begin{bmatrix} -\vartheta_{ss}\dfrac{\sigma_2}{E_{ss}} \\ \dfrac{\sigma_2}{E_{ss}} \end{bmatrix} \tag{15}$$

Eq. 16 compares the axial stress experienced by the PVDF piezoelectric sensor, which is more complex than that of the PZT sensor due to its anisotropic properties. The relationship between the substrate's Poisson ratio and the axial stress (T1) remains consistent: if the substrate's Poisson ratio is lower than the transverse Poisson ratio of the PVDF sensor, T1 increases, leading to a higher overall electrical displacement. Conversely, if the substrate's Poisson ratio is higher, T1 decreases, resulting in a lower output voltage.

The a_r and d_r values for the PVDF piezoelectric sensor are provided in Table 1, and the definitions are given in Eq. 17. These coefficients for the PZT piezoelectric sensor are equal to 1 due to the material's inherent symmetry.

$$a_r = \frac{E_2}{E_{21}} = \frac{\vartheta_2}{\vartheta_1} \text{and} d_r = \frac{d_{32}}{d_{31}} \tag{17}$$

3.2.2. Shear leg effect in FA PZT piezoelectric sensor

In practical applications, the bonding layer between the substrate and the FA piezoelectric sensor introduces some attenuation in strain transfer. Due to the finite thickness of the adhesive layer, the strain or strain gradient in the substrate is not completely transmitted to the sensor, a phenomenon known as the shear lag effect. To ensure accurate strain measurements, a correction for the shear lag effect, as presented by Crawley and de Luis [49], is applied. This correction factor is described in Eq. 18.

$$\frac{\partial^2\zeta}{\partial x^2} - \left[\left(\frac{G_{glue}}{E_{sen} \times t_{sen} \times t_{glue}}\right) + \left(\frac{4 \times G_{glue} \times w_{sen}}{E_{sub} \times w_{sub} \times t_{sub} \times t_{glue}}\right)\right]\zeta = 0 \tag{18}$$

Where $\zeta = \varepsilon_{Sen}/\varepsilon_{Sub}$, G is the shear modulus for the adhesive layer, and w and t represent the width and thickness, respectively. A solution for Eq. 19 is given as:

$$\zeta = A\cosh\Gamma x + B\sinh\Gamma x \tag{19}$$

Γ is a substitution defined in Eq. 20, and by applying the boundary conditions outlined in Eq. 21, ζ can be expressed as shown in Eq. 22.

$$\Gamma = \sqrt{\left(\frac{G_{glue}}{E_{sen} \times t_{sen} \times t_{glue}}\right) + \left(\frac{4 \times G_{glue} \times w_{sen}}{E_{sub} \times w_{sub} t_{sub} \times t_{glue}}\right)} \tag{20}$$

$$Bouandary\ conditions : \begin{cases} x = 0 \quad , \& \zeta = 0 \\ x = l_{sen}, \& \zeta = 0 \end{cases} \tag{21}$$

$$\zeta = \frac{\cosh\Gamma l_{sen} - 1}{\sinh\Gamma l_{sen}} \times \sinh\Gamma x - \cosh\Gamma x + 1 \tag{22}$$

By applying the dimensions to Eq. 22, the correction factors for ε_l (longitudinal strain) and ε_w (transverse strain) are computed and illustrated in Fig. 4 for varying adhesive layer thicknesses. The results indicate that strain transmission is the highest at the center of the sensor, with no strain transfer occurring at the edges. Furthermore, an increase in adhesive thickness leads to a greater reduction in strain transmission. The strain ε_l at the sensor's center ranges from 95–100 % of the substrate strain, while ε_w decreases significantly from 99 % to 76 %, influenced by the sensor's narrow width as the adhesive thickness increases from 5 to 100 μm. The maximum strain values shown in the figures represent the overall 2D strain transfer from the substrate to the sensor.

By applying the correction factor for the shear lag effect to the axial strain and substituting this into the expression for electrical displacement, the sensor output voltage (Eq. 11) as a function of applied strain $\left(\frac{\sigma_2}{E_{ss}}\right)$ can be expressed for both FA PZT and PVDF piezoelectric sensors in Eqs. 23 and 24.

$$v_{(t)_{FA\_PZT}} = \frac{A}{C} e^{\frac{-t}{\tau}} \int_0^T e^{\frac{t}{\tau}} \frac{d}{dt}\left(d_{31} T_{1_{PZT}} + d_{32} T_{1_{PZT}}\right) dt = \left\{\frac{d_{31} \times E_{PZT}}{\left(1 - \vartheta_{PZT}{}^2\right)}\left(\zeta_w(\vartheta_{PZT} - \vartheta_{ss}) + \zeta_l(1 - \vartheta_{PZT}\vartheta_{ss})\right)\right\} \frac{A}{C} e^{\frac{-t}{\tau}} \int_0^T e^{\frac{t}{\tau}} \frac{d}{dt}\left(\frac{\sigma_2}{E_{ss}}\right) dt \tag{23}$$

$$v_{(t)_{FA\_PVDF}} = \frac{A}{C} e^{\frac{-t}{\tau}} \int_0^T e^{\frac{t}{\tau}} \frac{d}{dt}\left(d_{31} T_{1_{PVDF}} + d_{32} T_{2_{PVDF}}\right) dt = \left\{\frac{d_{31} \times E_{1_{PVDF}}}{\left(1 - \vartheta_{1_{PVDF}}{}^2 a_r\right)}\left(\zeta_w(\vartheta_{1_{PVDF}} - \vartheta_{ss}) + \zeta_l d_r a_r (1 - \vartheta_{1_{PVDF}}\vartheta_{ss})\right)\right\} \frac{A}{C} e^{\frac{-t}{\tau}} \int_0^T e^{\frac{t}{\tau}} \frac{d}{dt}\left(\frac{\sigma_2}{E_{ss}}\right) dt \tag{24}$$

Where ζ_w and ζ_l are the shear lag correction factors and d_r is defined in Eq. 17.

3.2.3. Strain in TEA piezoelectric sensor

As discussed in the previous section, the performance of the sensor in the FA configuration is influenced by the substrate's Poisson ratio and the shear lag effect. To minimize the sensor's dependence on these substrate properties, the sensor can be attached at only two ends using a narrow adhesive layer, as illustrated in Fig. 1b. This configuration, TEA configuration, allows the sensor to primarily follow the substrate's uniaxial strain while exhibiting its own Poisson ratio behaviour in the direction perpendicular to the substrate's loading.

For the glue-covered area, the equations are similar to those in the FA configuration. In the TEA configuration, there are two regions: attached and non-attached areas. Since the electrode-covered area contributes to the electrical performance, Fig. 1b shows that the total electrode-covered area is 26 mm × 45.5 mm = 44.2 mm². In comparison, the glue-covered area is 26 mm × (6 mm – 4.3 mm) = 1.18 mm². The glue-covered proportion is $\left(\frac{1.183E-6}{44.2E-6} = 3.73\%\right)$, which is neglected. Therefore, governing equations for the TEA configuration can be written as Eqs. 25 and 26.

$$\begin{bmatrix} T_{1_{PZT}} \\ T_{2_{PZT}} \end{bmatrix} = \frac{E_{PZT}}{\left(1 - \vartheta_{PZT}{}^2\right)} \begin{bmatrix} 1 & \vartheta_{PZT} \\ \vartheta_{PZT} & 1 \end{bmatrix} \begin{bmatrix} 0 \\ \frac{\sigma_2}{E_{ss}} \end{bmatrix} \tag{25}$$

$$\begin{bmatrix} T_{1_{PVDF}} \\ T_{2_{PVDF}} \end{bmatrix} = \frac{E_{1_{PVDF}}}{\left(1 - \vartheta_{1_{PVDF}}\vartheta_{2_{PVDF}}\right)} \begin{bmatrix} 1 & \vartheta_{1_{PVDF}} \\ \vartheta_{2_{PVDF}} & \frac{E_{2_{PVDF}}}{E_{1_{PVDF}}} \end{bmatrix} \begin{bmatrix} 0 \\ \frac{\sigma_2}{E_{ss}} \end{bmatrix} \tag{26}$$

Eqs. 25 and 26 show no direct dependence on the substrate's Poisson ratio, suggesting that the TEA configuration significantly reduces sensitivity to the mechanical properties of the underlying structure. However, in practical applications, minor residual effects may still arise due to strain transfer at the bonded ends and properties of the adhesive layer. Additionally, the shear lag effect can be ignored due to the negligible contribution of the electrode-covered area to the electrical output. The piezoelectric output voltage as a function of strain for the TEA configuration, for both PZT and PVDF piezoelectric sensors, is presented in Eqs. 27 and 28.

$$v_{(t)_{TEA\_PZT}} = \frac{A}{C}e^{\frac{-t}{\tau}}\int_0^T e^{\frac{t}{\tau}}\quad\frac{d}{dt}\left(d_{31}T_{1_{PZT}}+d_{32}T_{1_{PZT}}\right)dt$$

$$=\left\{\frac{d_{31}\times E_{PZT}}{\left(1-\vartheta_{PZT}{}^2\right)}\left(\vartheta_{PZT}+1\right)\right\}\frac{A}{C}e^{\frac{-t}{\tau}}\int_0^T e^{\frac{t}{\tau}}\quad\frac{d}{dt}\left(\frac{\sigma_2}{E_{ss}}\right)dt \tag{27}$$

$$v_{(t)_{TEA\_PVDF}} = \frac{A}{C}e^{\frac{-t}{\tau}}\int_0^T e^{\frac{t}{\tau}}\quad\frac{d}{dt}\left(d_{31}T_{1_{PVDF}}+d_{32}T_{2_{PVDF}}\right)dt$$

$$=\left\{\frac{d_{31}\times E_{1_{PVDF}}}{\left(1-\vartheta_{1_{PVDF}}{}^2a_r\right)}\left(\vartheta_{1_{PVDF}}+d_ra_r\right)\right\}\frac{A}{C}e^{\frac{-t}{\tau}}\int_0^T e^{\frac{t}{\tau}}\quad\frac{d}{dt}\left(\frac{\sigma_2}{E_{ss}}\right)dt \tag{28}$$

4. Results and discussions

The analytical comparison of FA and TEA configurations (Eqs. 23, 24, 27, and 28) for both PZT and PVDF sensors—where PVDF is considered analytically only—under varying Poisson ratios of the sensors (0.3–0.4) and substrate (0–0.4), reveals that the TEA configuration is unaffected by the substrate's Poisson ratio. These Poisson ratio values are selected from the literature review for different ranges of piezoelectric sensors and engineering substrate structures such as aluminium, steel, reinforced concrete, etc. As illustrated in Fig. 5a, for structures with a Poisson ratio lower than that of the PZT piezoelectric sensor, the FA configuration with a PZT sensor generates a higher open-circuit voltage. Additionally, due to its anisotropic properties, the piezoelectric sensor performs better in the TEA configuration than in the FA configuration. Fig. 5a reflects a Poisson ratio for the piezoelectric sensors, based on variations found in the literature. Examining the strain experienced by both PZT and PVDF sensors in different attachment modes, Fig. 5b highlights how the shear lag effect in the FA configuration reduces the strain level, it also represents a share of d_{31} and d_{32} in each sensor. As expected, the PZT sensor generates a significantly higher voltage than the PVDF sensor (for the same dimensions), due to the higher piezoelectric coefficients, making it a more suitable choice for high-sensitivity applications. As a result, the experimental portion of this study was conducted using the PZT piezoelectric sensor.

Fig. 6a illustrates the strain distribution along the structure in the longitudinal direction, highlighting the major strain. In the FA configuration, the PZT piezoelectric sensor experiences nearly the same strain as the substrate. However, Fig. 6b, which presents the average strain level as a function of applied stress, reveals the average longitudinal and transverse strain across multiple points on the sensors and substrate. The strain in the FA configuration is slightly lower than that in the substrate, which could be attributed to the shear lag effect.

In contrast, the TEA configuration in Fig. 6a shows an uneven strain distribution, likely due to imperfect attachment on the side with the sensor wires. The bottom left corner of the TEA sensor shows significant strain where it should match the substrate. On the opposite side, the attachment appears more secure, and higher transverse strain is evident, which can be explained by the PZT sensor's higher Poisson ratio than the substrate. Fig. 6b confirms this observation with higher transverse strain in the TEA configuration.

A closer examination of the major strain distribution reveals two areas of significant stretching, circled and labelled A1 and A2 in the TEA configuration. These areas are likely attributed to experimental errors. A1 is likely due to imperfect bonding, while A2 may be caused by the presence of a softer encapsulation layer at the edge of the adhesive layer (as shown in Fig. 1b), where the PZT material and electrodes are absent. These imperfections contribute to a reduction in longitudinal strain, as clearly illustrated in Fig. 6b. Despite these experimental errors, Fig. 6b

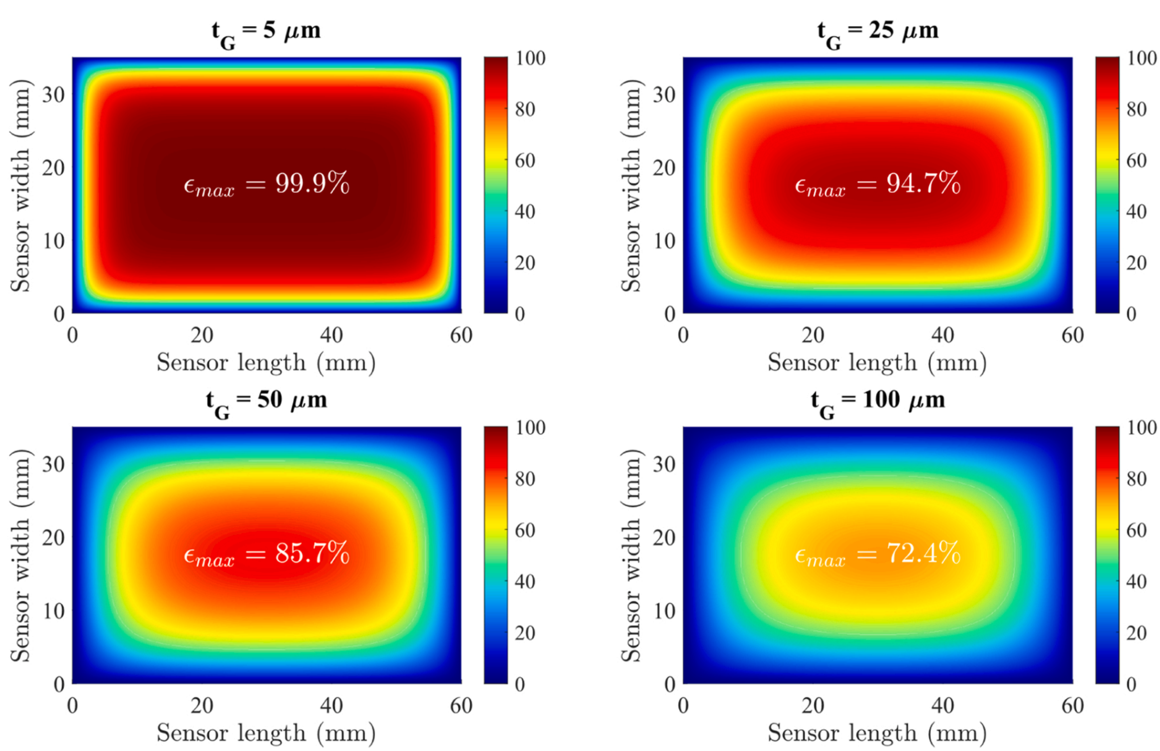

Fig. 4. Two-dimensional strain maps illustrating the shear lag correction factors for both longitudinal and transverse strain distributions across the sensor, evaluated for four different adhesive layer thicknesses (t_G).

demonstrates a strong correlation between the experimental measurements and the theoretical predictions, confirming the overall validity of the results. However, minor discrepancies between analytical and experimental results suggest the need for further investigation into influencing factors such as the mechanical properties and thickness of the adhesive layer, possible temperature variations during testing, and the long-term durability or drift of piezoelectric sensors under cyclic loading. These effects, although not dominant in the current setup, could become more pronounced in extended monitoring applications.

Fig. 7 compares the experimental (PZT) and analytical (PZT and PVDF) results of sensor output voltage under cyclic tensile loading, showing a good agreement. Regarding the error in the TEA configuration shown in Fig. 6, Fig. 7a also reveals that the analytical results predict a higher output for TEA compared to the experimental results.

Another difference between the analytical and experimental results is that the analytical model shows FA having a lower output than TEA, with the ratio between FA and TEA remaining constant, as illustrated in Fig. 7b. However, in the experimental results, at lower loading frequencies, the FA configuration agrees with the analytical model, but as the loading frequency increases, the FA configuration demonstrates a higher output. The difference between experimental and analytical results grows as the loading frequency increases. This can be explained by considering the dynamic sensitivity of piezoelectric sensors, as defined in Eq. 11.

The FA sensor closely follows the substrate's deformation, whereas the TEA sensor primarily tracks the substrate's uniaxial tension. During the unloading and release process, the TEA sensor is influenced by the slower relaxation time of the PZT material, which exhibits time-dependent behaviour due to its viscoelastic and piezoelectric contrast [33,50–53], the FA sensor is constrained by the substrate's relaxation time. Given that stainless steel has higher stiffness and negligible viscoelasticity in the elastic region, its relaxation time is much shorter compared to the PZT piezoelectric sensor, which responds more slowly due to domain switching and internal dipole [54] results in the FA sensor undergoing more dynamic deformation during the unloading process, leading to higher output at higher frequencies compared to the TEA configuration [55]. In addition to the FA configuration's dependency on the substrate's Poisson ratio, its faster relaxation behaviour contributes

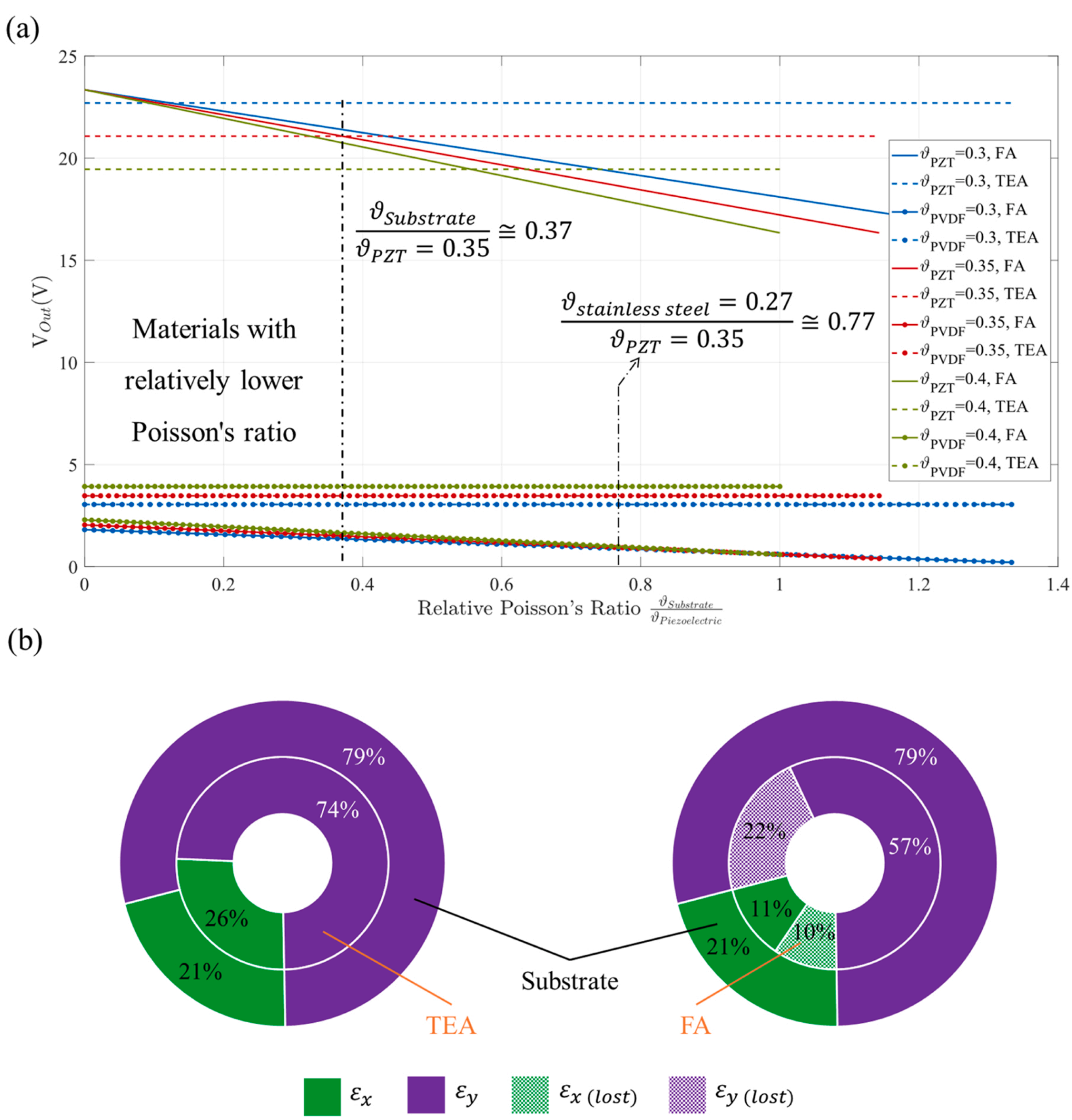

Fig. 5. (a) Sensor output voltage versus relative Poisson ratio for PZT and PVDF in FA and TEA configurations; (b) Applied versus transferred strain, showing the effect of shear lag in each setup.

to the complexity of the sensor's voltage-strain relation.

5. Conclusion

This study demonstrates that piezoelectric sensors can accurately measure strain in substrate structures, with a comprehensive investigation into the voltage-strain relationship for both PZT and PVDF piezoelectric sensors. The research explored the fundamentals of piezoelectricity, electrical equivalent circuits, and solid mechanics for two attachment configurations: FA and TEA. Analytical results indicated that the attachment method significantly influences the sensor's behaviour and its dependency on the substrate. In the FA configuration, the substrate's Poisson ratio affects the sensor's output voltage, and experimental findings show that the substrate's elasticity introduces additional nonlinearity in the voltage–strain relationship compared to the TEA configuration. This is in addition to the intrinsic nonlinear behaviour of the piezoelectric material itself.

When using piezoelectric sensors for strain measurements, at least two sensors are required to capture strains in different coordinates, and the adhesion layer, as well as the substrate's mechanical properties, must be carefully considered. Changes in the substrate's properties over time can lead to inaccuracies in measurement. To reduce this dependency, it is proposed to attach the piezoelectric sensor only at its ends, minimizing the influence of the substrate's Poisson ratio and the shear lag effect. Further studies should explore alternative adhesives and flexible mounting techniques to enhance sensor stability while preserving measurement accuracy, particularly under long-term operational conditions. The developed equations show that the TEA configuration captures uniaxial strain independently of the substrate's properties. Experimentally, it is recommended that in the TEA configuration, the

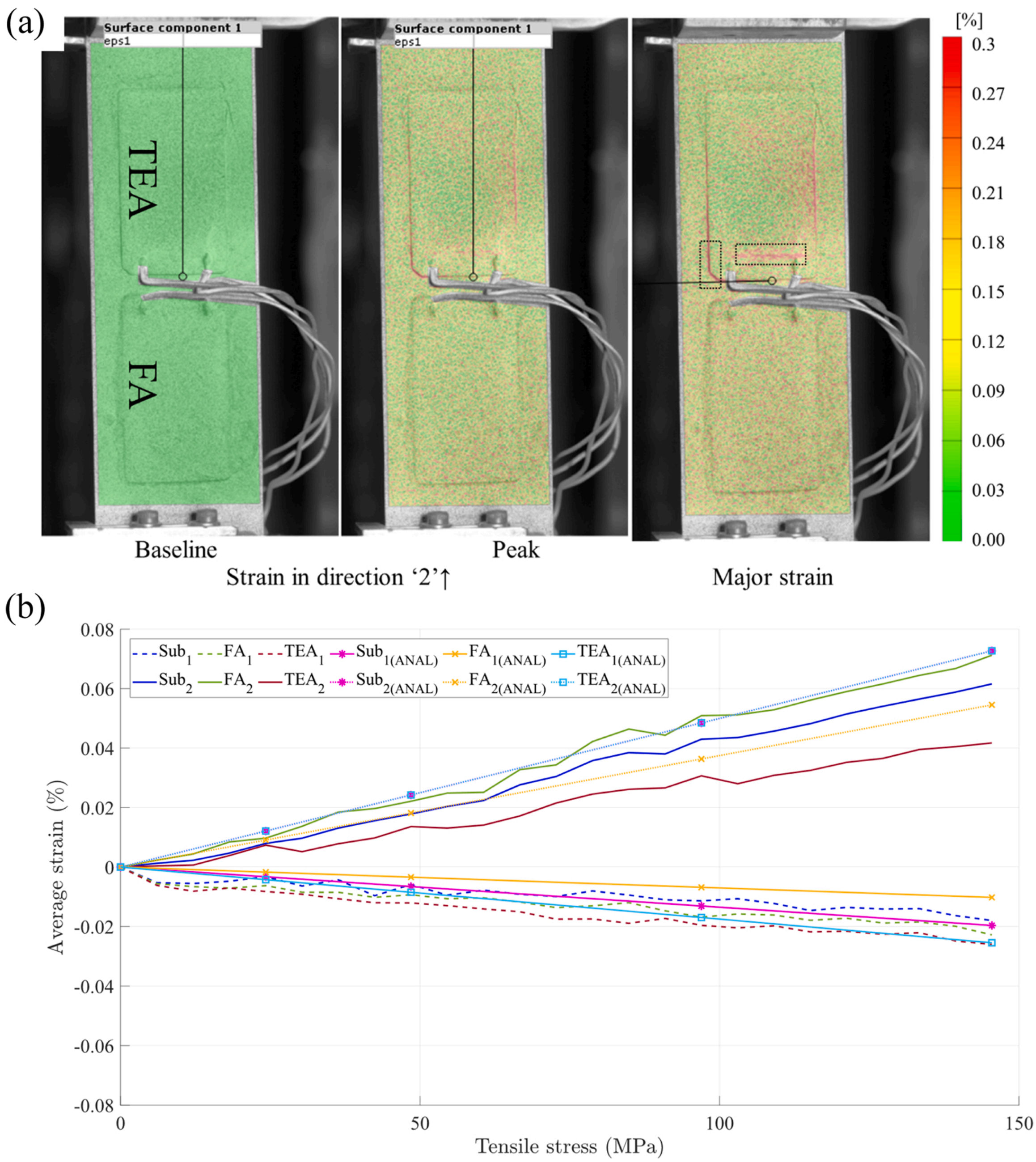

Fig. 6. DIC measurements of PZT sensors in FA and TEA configurations: (a) Longitudinal strain distribution at baseline and 145 MPa; (b) Transverse and longitudinal strain vs. tensile stress for both configurations, compared with analytical results.

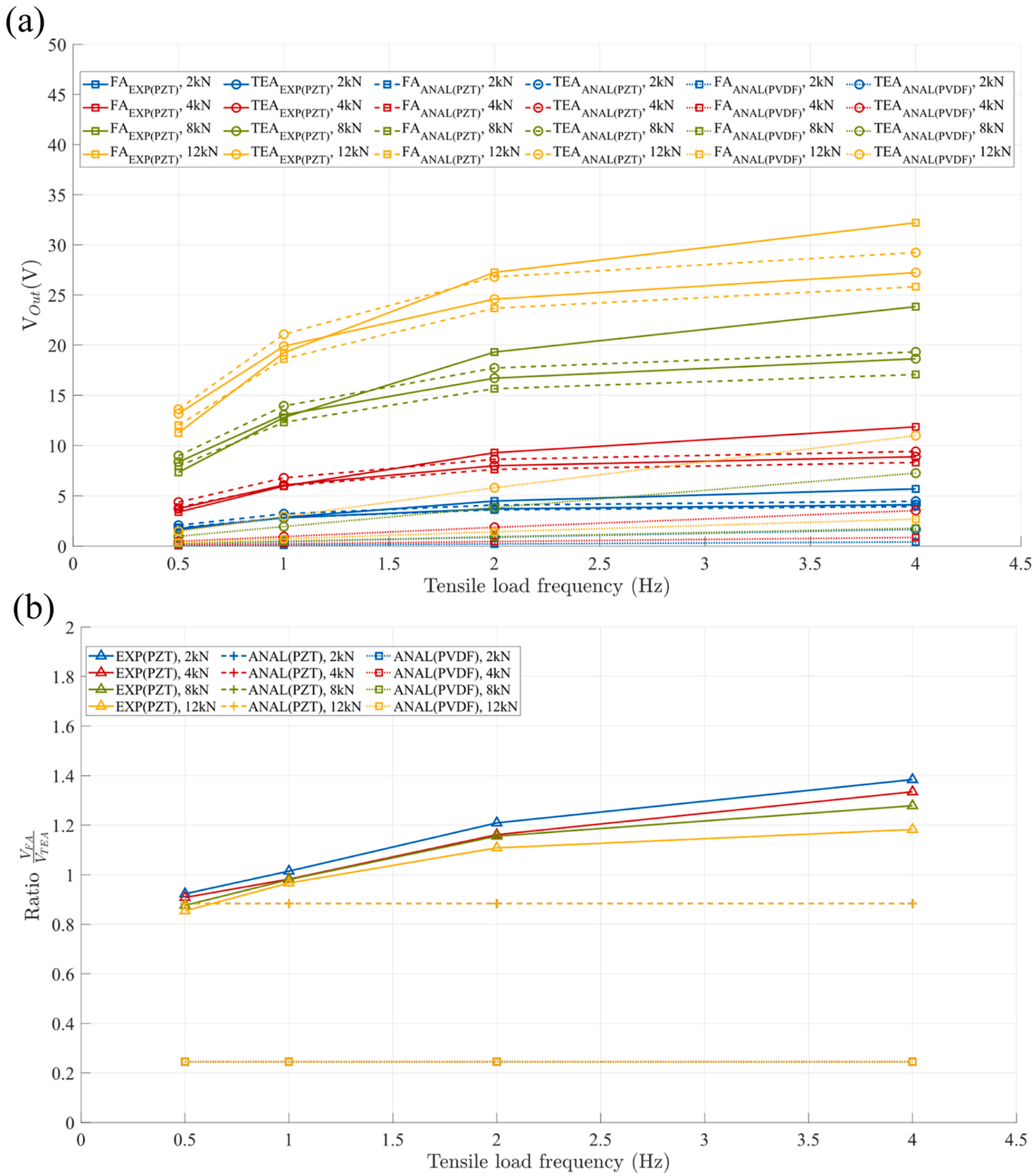

Fig. 7. (a) Output voltage of PZT and PVDF sensors vs. loading frequency under varying tensile loads in FA and TEA configurations, comparing experimental results (PZT) with analytical predictions (PZT and PVDF); (b) Comparison of FA and TEA configurations for PZT (experimental and analytical) and PVDF (analytical only).

adhesive area should extend to the boundary of the electrode-covered area to avoid uneven strain distribution.

While the TEA configuration offers advantages, analytical results reveal that the FA configuration produces higher output voltage for substrates with relatively lower Poisson ratios. The PVDF piezoelectric sensor, due to its lower piezoelectric coefficients, exhibited a lower output voltage compared to the PZT sensor, as predicted by the analytical model. Additionally, the PVDF sensor displayed distinct behaviour with varying substrate Poisson ratios, with the TEA configuration generating higher output voltage across all ranges due to the sensor's inherent orthotropic symmetry.

The findings of this study provide valuable insights for improving the application of piezoelectric sensors in uniaxial strain measurements and contribute to a deeper understanding of their behaviour in structural strain monitoring.

CRediT authorship contribution statement

Ghaderiaram Aliakbar: Writing – original draft, Visualization, Validation, Software, Project administration, Methodology, Investigation, Funding acquisition, Formal analysis, Data curation, Conceptualization. **Vafa Navid:** Writing – review & editing, Visualization, Software, Funding acquisition, Formal analysis. **Schlangen Erik:** Writing – review & editing, Supervision, Resources, Project administration. **Fotouhi**

Mohammad: Writing – review & editing, Validation, Supervision, Resources, Project administration, Methodology, Investigation, Formal analysis.

Declaration of Generative AI and AI-assisted technologies in the writing process

During the preparation of this work, the authors used ChatGPT to improve English language and writing clarity. After using this tool, the authors reviewed and edited the content as needed and take full responsibility for the content of the publication.

Declaration of Competing Interest

The authors declare that they have no known competing financial interests or personal relationships that could have appeared to influence the work reported in this paper.

Data Availability

Data will be made available on request.

References

[1] Y.E. Zhou, M. Asce, Assessment of bridge remaining fatigue life through field strain measurement, Proc. Struct. Congr. Expo. (2005) 129–139, https://doi.org/10.1061/(ASCE)1084-0702(2006)11:6(737).
[2] M.R. Saberi, et al., Bridge fatigue service-life estimation using operational strain measurements, J. Bridg. Eng. 21 (5) (2016), https://doi.org/10.1061/(ASCE)BE.1943-5592.0000860.
[3] J. Pacheco, F. Pimenta, S. Pereira, Á. Cunha, F. Magalhães, Fatigue assessment of wind turbine towers: review of processing strategies with illustrative case study, vol. 15, no. 13, p. 4782, Jun. 2022, Energies 15 (2022) *4782*, https://doi.org/10.3390/EN15134782.
[4] N. Periši ć, P.H. Kirkegaard, U.T. Tygesen, Load identification of offshore platform for fatigue life estimation, Conf. Proc. Soc. Exp. Mech. Ser. 5 (2014) 99–109, https://doi.org/10.1007/978-3-319-04570-2_11/FIGURES/7.
[5] X.W. Ye, Y.Q. Ni, K.Y. Wong, J.M. Ko, Statistical analysis of stress spectra for fatigue life assessment of steel bridges with structural health monitoring data, Eng. Struct. 45 (2012) 166–176, https://doi.org/10.1016/J.ENGSTRUCT.2012.06.016.
[6] X.W. Ye, Y.H. Su, J.P. Han, A state-of-the-art review on fatigue life assessment of steel bridges, Math. Probl. Eng. 2014 (1) (2014) 956473, https://doi.org/10.1155/2014/956473.
[7] Y. Yao, B. Glisic, Detection of steel fatigue cracks with strain sensing sheets based on large area electronics, Sensors 15 (2015) 8088–8108, https://doi.org/10.3390/s150408088.
[8] W.B. Chen, W.Q. Feng, J.H. Yin, L. Borana, LVDTs-based radial strain measurement system for static and cyclic behavior of geomaterials, Measurement 155 (2020) 107526, https://doi.org/10.1016/J.MEASUREMENT.2020.107526.
[9] V. Goanta, Extensometer for determining strains on a tensile and torsion simultaneous load, Sensors 20 (2) (2020), https://doi.org/10.3390/s20020385.
[10] Z. Liang, et al., FBG-based strain monitoring and temperature compensation for composite tank, Aerosp. Sci. Technol. 127 (2022) 107724, https://doi.org/10.1016/J.AST.2022.107724.
[11] P. Corigliano, V. Crupi, X. Pei, P. Dong, DIC-based structural strain approach for low-cycle fatigue assessment of AA 5083 welded joints, Theor. Appl. Fract. Mech. 116 (2021) 103090, https://doi.org/10.1016/J.TAFMEC.2021.103090.
[12] X. Wang, et al., Real-time monitoring of asphalt pavement structure fatigue response based on tri-axis accelerometer, Int. J. Pavement Eng. 25 (1) (2024), https://doi.org/10.1080/10298436.2024.2308158.
[13] Z. Huang, Z. Duan, Q. Huang, Z. Yuan, Y. Jiang, H. Tai, A facilely fabricated electrochemical self-powered pressure sensor for multifunctional applications, J. Mater. Chem. C 12 (45) (2024) 18320–18326, https://doi.org/10.1039/D4TC03434A.
[14] Q. Huang, et al., Ion gradient induced self-powered flexible pressure sensor, Chem. Eng. J. 490 (2024) 151660, https://doi.org/10.1016/J.CEJ.2024.151660.
[15] X. Feng, et al., Amorphous carbon derived from daily carbon ink for wide detection range, low-cost, eco-friendly and flexible pressure sensor, Mater. Chem. Phys. 321 (2024) 129489, https://doi.org/10.1016/J.MATCHEMPHYS.2024.129489.
[16] C. Wang, et al., Design, fabrication, and characterization of 1-3 piezoelectric composite air-coupled ultrasonic transducers with micro-membrane filter matching layer, Sens. Actuators A Phys. (2024) 115955, https://doi.org/10.1016/J.SNA.2024.115955.
[17] N. Toyama, J. Takatsubo, An investigation of non-linear elastic behavior of CFRP laminates and strain measurement using Lamb waves, Compos. Sci. Technol. 64 (16) (2004) 2509–2516, https://doi.org/10.1016/J.COMPSCITECH.2004.05.007.
[18] R. Zahoor, et al., Lamb wave detection for structural health monitoring using a ϕ-OTDR system, Sensors 22 (2022) 5962, https://doi.org/10.3390/S22165962.
[19] K.A. Kalteremidou, D.G. Aggelis, D.Van Hemelrijck, L. Pyl, On the use of acoustic emission to identify the dominant stress/strain component in carbon/epoxy composite materials, Mech. Res. Commun. 111 (2021) 103663, https://doi.org/10.1016/J.MECHRESCOM.2021.103663.
[20] H. Kim, et al., Numerical evaluation of acoustic emission (AE) sensors by lead-zirconate-titanate (PZT) geometric design, Sens. Actuators A Phys. 366 (2024) 115031, https://doi.org/10.1016/J.SNA.2024.115031.
[21] A. Ghaderiaram, E. Schlangen, M. Fotouhi, Structural fatigue life monitoring with piezoelectric-based sensors: fundamentals, current advances, and future directions, Sensors 25 (2025) 334, https://doi.org/10.3390/S25020334.
[22] Y. Yang, X. Wei, W. Yao, J. Lan, Broadband electrical impedance matching of sandwiched piezoelectric ultrasonic transducers for structural health monitoring of the rail in-service, Sens. Actuators A Phys. 364 (2023) 114819, https://doi.org/10.1016/J.SNA.2023.114819.
[23] E. Matsumoto, S. Biwa, K. Katsumi, Y. Omoto, K. Iguchi, T. Shibata, Surface strain sensing with polymer piezoelectric film, NDT E Int. 37 (1) (2004) 57–64, https://doi.org/10.1016/J.NDTEINT.2003.08.006.
[24] A.K. Ramanathan, L.M. Headings, M.J. Dapino, Near static strain measurement with piezoelectric films, Sens. Actuators A Phys. 301 (2020) 111654, https://doi.org/10.1016/J.SNA.2019.111654.
[25] J. Sirohi, I. Chopra, Fundamental understanding of piezoelectric strain sensors, http://dx. doi. Org. /10. 1106/8BFB-GC8P-XQ47-YCQ0 11 (4) (2000) 246–257, https://doi.org/10.1106/8BFB-GC8P-XQ47-YCQ0.
[26] L. Yan Voon, R. Melnik, and M. Willatzen, Strain measurement on stiff structures: Experimental evaluation of three integrated measurement principles, doi: 10.1088/0964-1726/21/6/064008.
[27] Y.K. Yong, A.J. Fleming, S.O. Moheimani, A novel piezoelectric strain sensor for simultaneous damping and tracking control of a high-speed nanopositioner, IEEE/ASME Trans. Mechatron. 18 (3) (2013) 1113–1121, https://doi.org/10.1109/TMECH.2012.2193895.
[28] W. Huang, F.G. Yuan, X. Jiang, Flexoelectric strain gradient sensing, 3, Elsevier Ltd, 2016, https://doi.org/10.1016/B978-0-08-100148-6.00006-8.
[29] C. Wallbrink, J.M. Hughes, A. Kotousov, Application of an advanced piezoelectric strain sensor for crack closure measurement, Int. J. Fatigue 167 (2023) 107286, https://doi.org/10.1016/J.IJFATIGUE.2022.107286.
[30] K.L. Ganapathi, et al., Temperature-dependent mechanical depolarization of ferroelectric ceramics, J. Phys. D. Appl. Phys. 43 (17) (2010) 175501, https://doi.org/10.1088/0022-3727/43/17/175501.
[31] Y. Chen, S. Xie, Q. Wang, L. Fu, R. Nie, J. Zhu, Correlation between microstructural evolutions and electrical/mechanical behaviors in Nb/Ce co-doped Pb (Zr0.52Ti0.48)O3 ceramics at different sintering temperatures, Mater. Res. Bull. 94 (2017) 174–182, https://doi.org/10.1016/J.MATERRESBULL.2017.05.045.
[32] H. Zheng, Y. Li, D. He, P. Wen, S.L. Yan, High-performance flexible piezoelectric sensors based on honeycomb graphene macro-film exploiting auxetic mechanical property, Sens. Actuators A Phys. 372 (2024) 115374, https://doi.org/10.1016/J.SNA.2024.115374.
[33] M. Krommer, P. Berik, Y. Vetyukov, A. Benjeddou, Piezoelectric d 15 shear-response-based torsion actuation mechanism: An exact 3D Saint-Venant type solution, Int. J. Smart Nano Mater. 3 (2) (2012) 82–102, https://doi.org/10.1080/19475411.2011.649807.
[34] S. Fotouhi, R. Akrami, K. Ferreira-Green, G.A.M. Naser, M. Fotouhi, C. Fragassa, Piezoelectric PVDF sensor as a reliable device for strain/load monitoring of engineering structures, IOP Conf. Ser. Mater. Sci. Eng. 659 (1) (2019), https://doi.org/10.1088/1757-899X/659/1/012085.
[35] A.K. Ramanathan, L.M. Headings, M.J. Dapino, Near static strain measurement with piezoelectric films, Sens. Actuators A Phys. 301 (2020) 111654, https://doi.org/10.1016/j.sna.2019.111654.
[36] J. Zhang, A. Nyilas, B. Obst, New technique for measuring the dynamic Young's modulus between 295 and 6 K, Cryogenius 31 (10) (1991) 884–889, https://doi.org/10.1016/0011-2275(91)90022-O.
[37] A. Ghaderiaram, E. Schlangen, M. Fotouhi, Analysis of PZT piezoelectric sensors in buckling mode for dynamic strain measurement, e-J. Nondestruct. Test. 29 (7) (2024) 1–8, https://doi.org/10.58286/29596.
[38] A. Ghaderiaram, R. Mohammadi, E. Schlangen, M. Fotouhi, Development of an innovative extension for fatigue life monitoring using a piezoelectric sensor, Procedia Struct. Integr. 52 (2024) 570–582, https://doi.org/10.1016/j.prostr.2023.12.057.
[39] S.J. Rupitsch, Piezoelectric Sensors and Actuators, Springer Berlin Heidelberg, Berlin, Heidelberg, 2019, https://doi.org/10.1007/978-3-662-57534-5.
[40] M.G. Cain and M. Stewart, Standards for Piezoelectric and Ferroelectric Ceramics, pp. 267–275, 2014, doi: 10.1007/978-1-4020-9311-1_12.
[41] V.T. Rathod, A review of electric impedance matching techniques for piezoelectric sensors, actuators and transducers, Electron 8 (2019) 169, https://doi.org/10.3390/ELECTRONICS8020169.
[42] M.J. Guan, W.H. Liao, On the equivalent circuit models of piezoelectric ceramics, Ferroelectrics 386 (1) (2009) 77–87, https://doi.org/10.1080/00150190902961439.
[43] J. Chen, N. Nabulsi, W. Wang, J.Y. Kim, M.K. Kwon, J.H. Ryou, Output characteristics of thin-film flexible piezoelectric generators: a numerical and experimental investigation, Appl. Energy 255 (2019) 113856, https://doi.org/10.1016/J.APENERGY.2019.113856.
[44] R. Haynes, J. Cline, B. Shonkwiler, E. Armanios, On plane stress and plane strain in classical lamination theory, Compos. Sci. Technol. 127 (2016) 20–27, https://doi.org/10.1016/J.COMPSCITECH.2016.02.010.

[45] Y. Fujimoto, E. Shintaku, G. Pirker, G. Liu, Piezoelectric sensor for stress intensity factor measurement of two dimensional cracks, Eng. Fract. Mech. 70 (9) (2003) 1203–1218, https://doi.org/10.1016/S0013-7944(02)00091-7.
[46] V.V. Varadan, Y.R. Roh, V.K. Varadan, R.H. Tancrell, Measurement of all the elastic and dielectric constants of poled PVDF films, Ultrason. Symp. Proc. 2 (1989) 727–730, https://doi.org/10.1109/ULTSYM.1989.67082.
[47] Y. Yu, et al., An investigation of thin PVDF films as fluctuating-strain-measuring and damage-monitoring devices Characterizing piezoelectric properties of PVDF film under extreme loadings An investigation of thin PVDF films 1 as fluctuating-strain-measuring and damage-monitoring devices, Smart Mater. Strud 2 (1993) 208–216.
[48] G.M. Odegard, Constitutive modeling of piezoelectric polymer composites, Acta Mater. 52 (18) (2004) 5315–5330, https://doi.org/10.1016/J.ACTAMAT.2004.07.037.
[49] E.F. Crawley, J. De Luisj, S. Ma, and / Eq, Use of Piezoelectric Actuators as Elements of Intelligent Structures < *31 E F F, F 2 G IB, vol. 25, doi: 10.2514/3.9792.
[50] H.M. Ledbetter, M.W. Austin, Effects of carbon and nitrogen on the elastic constants of AISI type 304 stainless steel, Mater. Sci. Eng. 70 (C) (1985) 143–149, https://doi.org/10.1016/0025-5416(85)90275-7.
[51] T. Ito, T. Nishi, T. Umegaki, H. Hida, I. Kanno, The piezoelectric PZT thin films deposited on metal substrates, IOP Publ. IOP Conf. Ser. J. Phys. Conf. Ser. 1052 (2017) 12094, https://doi.org/10.1088/1742-6596/1052/1/012094.
[52] M. Selten, G.A. Schneider, V. Knoblauch, R.M. McMeeking, On the evolution of the linear material properties of PZT during loading history—an experimental study, Int. J. Solids Struct. 42 (13) (2005) 3953–3966, https://doi.org/10.1016/J.IJSOLSTR.2004.12.004.
[53] A.Y. Malkin, A.I. Isayev, VISCOELASTICITY, Rheol. Concepts Methods Appl. (2012) 43–126, https://doi.org/10.1016/B978-1-895198-49-2.50007-4.
[54] K. Morimoto, I. Kanno, K. Wasa, H. Kotera, High-efficiency piezoelectric energy harvesters of c-axis-oriented epitaxial PZT films transferred onto stainless steel cantilevers, Sens. Actuators A Phys. 163 (1) (2010) 428–432, https://doi.org/10.1016/J.SNA.2010.06.028.
[55] I. Kanno, et al., High efficiency energy harvester of transferred epitaxial PZT films on stainless steel sheets, Proc. IEEE Int. Conf. Micro Electro Mech. Syst. (2010) 152–155, https://doi.org/10.1109/MEMSYS.2010.5442542.

Aliakbar Ghaderiaram is a PhD candidate at TU Delft, specializing in self-powered sensor node design for structural health monitoring. His research focuses on the design and development of wireless sensor nodes using piezoelectric materials to monitor fatigue life in engineering structures. He holds a background in electronic engineering and integrates signal processing, embedded systems, energy harvesters and smart materials into advanced monitoring solutions.

Dr. Navid Vafa holds a Bachelor's and a first Master's degree in Civil Engineering from Iran, where he focused on dissipative devices for steel frames. He later earned a second Master's degree full grade from Politecnico di Milano, Italy, specializing in numerical modeling of masonry structures. He completed his PhD cum laude at Politecnico di Milano on the seismic retrofitting of masonry using post-installed systems. Currently, he is a postdoctoral researcher at TU Delft, focusing on the seismic behavior and retrofitting of masonry structures made of calcium silicate.

Professor Erik Schlangen is a leading expert in self-healing materials, experimental micromechanics and structural health monitoring. He holds the Chair of Experimental Micromechanics at TU Delft and directs the Microlab in the Faculty of Civil Engineering and Geosciences. His research focuses on fracture mechanics, durability, and 3D concrete printing. Schlangen is best known for developing self-healing asphalt using steel wool fibers and induction heating. With over 250 publications and international recognition, including a TED talk, he actively contributes to education and outreach in engineering.

Dr. Mohammad Fotouhi is the director of the Material Health Monitoring group and an Associate Professor at TU Delft's Faculty of Civil Engineering and Geosciences. With over 180 scientific papers published in the fields of Composite Materials and Structural Health Monitoring, Dr. Fotouhi is a globally recognized expert in these areas. He has secured prestigious grants, including Open Technology and Vidi fellowship from the Dutch Research Council (NWO), to advance the development of next-generation composite materials. He also serves on the editorial boards of *Composite Materials*, the *Journal of Engineering and Technology*, and *IEEE Sensors Review*.